

Smart wing rotation and trailing-edge vortices enable high frequency mosquito flight

Richard J. Bomphrey¹, Toshiyuki Nakata^{1,2}, Nathan Phillips¹ & Simon M. Walker³

Mosquitoes exhibit unusual wing kinematics; their long, slender wings flap at remarkably high frequencies for their size (>800 Hz) and with lower stroke amplitudes than any other insect group¹. This shifts weight support away from the translation-dominated, aerodynamic mechanisms used by most insects², as well as by helicopters and aeroplanes, towards poorly understood rotational mechanisms that occur when pitching at the end of each half-stroke. Here we report free-flight mosquito wing kinematics, solve the full Navier–Stokes equations using computational fluid dynamics with overset grids, and validate our results with *in vivo* flow measurements. We show that, although mosquitoes use familiar separated flow patterns, much of the aerodynamic force that supports their weight is generated in a manner unlike any previously described for a flying animal. There are three key features: leading-edge vortices (a well-known mechanism that appears to be almost ubiquitous in insect flight), trailing-edge vortices caused by a form of wake capture at stroke reversal, and rotational drag. The two new elements are largely independent of the wing velocity, instead relying on rapid changes in the pitch angle (wing rotation) at the end of each half-stroke, and they are therefore relatively immune to the shallow flapping amplitude. Moreover, these mechanisms are particularly well suited to high aspect ratio mosquito wings.

Mosquitoes disperse, find mates, lay eggs and seek hosts in flight, but their small size and exceedingly high wingbeat frequencies present a substantial challenge for biomechanical measurements. To test our prediction that mosquitoes shift lift generation away from the translational phase of the wingbeat and rely more heavily on the pitching rotation phases at the end of each half-stroke (Fig. 1), we measured the wing motion and simulated the resulting aerodynamics of the southern house mosquito (*Culex quinquefasciatus*; Supplementary Video 1).

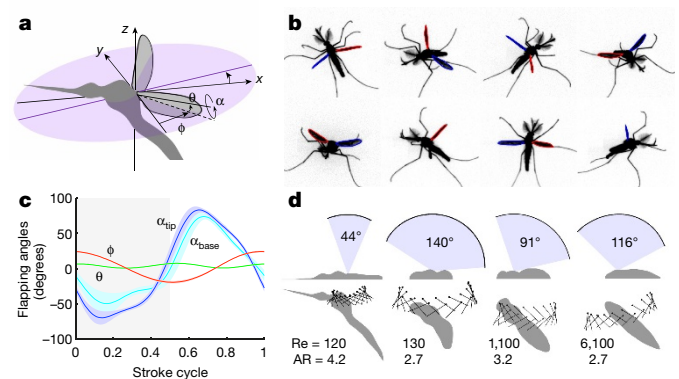


Figure 1 | Low-amplitude mosquito kinematics. **a**, Three axes and angles that define flapping wing kinematics; stroke position, φ (within the stroke plane, purple), wing pitch angle, α and deviation angle, θ . **b**, Eight views of a *C. quinquefasciatus* mosquito, showing automated extraction of wing outlines. **c**, Standardized stroke cycle kinematics from one individual (mean \pm s.d.; $n = 33$ wingbeats). Pitch angle, α , is shown for the base and tip of the wing to highlight longitudinal twist and pitching rotations that are important for unsteady aerodynamics. **d**, Dorsal (top) and lateral (bottom) views of characteristic motions ($R = 0.75$ wing length) for, left-to-right, mosquito, fruit fly¹⁸, honeybee²⁰ and hawk moth²¹. Reynolds numbers (Re ; based on mean tip velocity and mean chord length) and aspect ratios (AR) for each insect are given^{18,22,23}.

We confirm that mosquitoes have a diminished reliance on leading-edge vortices, an aerodynamic phenomenon that augments lift forces for insects^{3–8}, birds^{9,10} and bats¹¹ during wing translation. The effect of leading-edge vortices is to generate sufficient lift with

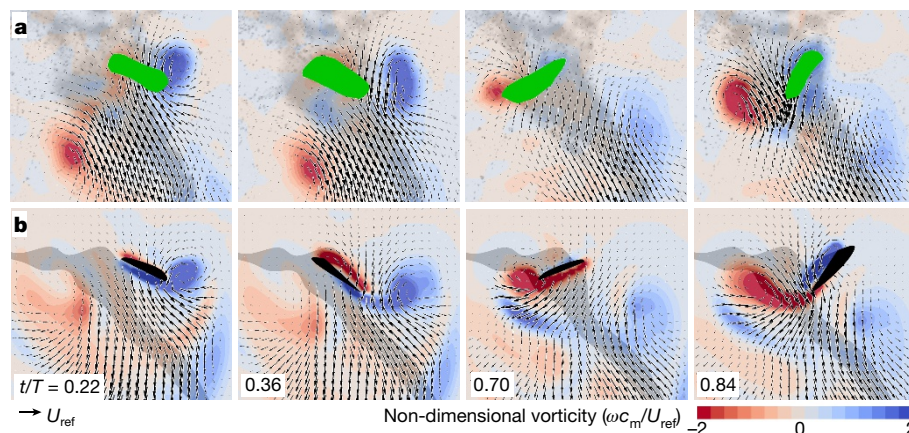


Figure 2 | Validation of CFD with PIV quantitative flow fields. **a**, **b**, Left-to-right, end of pronation ($t/T = 0.22$), late downstroke ($t/T = 0.36$), end of supination ($t/T = 0.70$) and late upstroke ($t/T = 0.84$); green shading shows areas of no data. Red and blue patches show

clockwise and anticlockwise vorticity. Flow velocity field planes are shown at $R = 0.5$ wing length for both CFD (**a**) and PIV (**b**). U_{ref} = reference velocity, ω = vorticity, c_m = mean chord length.

¹Structure and Motion Laboratory, Royal Veterinary College, University of London, Hatfield AL9 7TA, UK. ²Graduate School of Engineering, Chiba University, 1-33, Yayoi-cho, Inage-ku, Chiba-shi, Chiba 263-8522 Japan. ³Department of Zoology, University of Oxford, Oxford OX1 3PS, UK.

smaller wings; a clear advantage for flying taxa. Instead, we observed lift enhancement through two mechanisms that are exclusive to mosquitoes thus far; (i) lift enhancement due to a trailing-edge vortex captured during stroke reversal and (ii) partial weight support due to a newly described rotational effect at the end of each half-stroke. The latter mechanism, rotational drag, has been postulated previously^{12,13} but, here, is mediated by exquisitely timed kinematic patterns that cause a leading to trailing edge shift of the pitching axis during stroke reversal.

Our analysis of the free-flight kinematics of male *Culex* mosquitoes (Fig. 1a–c) revealed that they flapped their wings at frequencies of 717 ± 59 Hz (mean \pm one s.d.) and with amplitudes of just $39^\circ \pm 4^\circ$, which is less than half the smallest amplitude yet measured for any hovering animal, despite operating at similar scales to fruit flies (Fig. 1d). The stereotypically low amplitudes we measured mean that the 75% radial position of the wing travels just two chord lengths between stroke reversals. This, in turn, affects the aerodynamics and means that the fluid mechanics assumption that wings act like sweeping helicopter blades no longer holds¹⁴.

Our simulations of forces, torques, power expenditure and flow fields show great consistency, with the aerodynamic features being entirely robust to the wide variety of body velocities and wing kinematics within the behavioural repertoire that we measured (Extended Data Fig. 1). We re-validated the computational fluid dynamics (CFD) solver using particle image velocimetry, and found that the corresponding flow fields matched both qualitatively and quantitatively (Fig. 2).

The three distinct aerodynamic mechanisms occur sequentially during the stroke cycle, each used on both the downstroke and the upstroke: the trailing-edge vortex due to wake capture, the leading-edge vortex, and rotational drag. We present one mosquito by way of example (M08; Fig. 1), although every mosquito we measured exhibited each of these aerodynamic mechanisms (Extended Data Figs 2–6). Five key instants, marked t_1 – t_5 , are highlighted on the aerodynamic force traces (Fig. 3a). The first key instant (t_1) corresponds to a peak in lift force early in the downstroke, shortly after pronation, (Fig. 3a, t_1) due to a strong trailing-edge vortex bound to the hind portion of the wing (Fig. 3f). The trailing-edge vortex forms as the high-velocity induced flow from the preceding upstroke separates as it encounters the trailing edge at a higher angle of attack than in other insects (Extended Data Fig. 7). The trailing edge has very low ground speed at this moment but, under the influence of the upstroke wake, the airspeed and pressure gradient are sufficient for the shear layer to roll up into a coherent attached vortex. As it does so, a region of intense negative pressure forms that contributes to weight support.

The trailing-edge vortex is a form of wake capture as it is dependent on flow that is induced during the previous half-stroke. However, it is fundamentally distinct from previously described wake capture effects because a wake structure forms as the flow first encounters the trailing edge of the wing. This contrasts with the simpler case of augmentation or reorientation of lift generated by a forward-translating wing. The resultant flow pattern is notably reminiscent of the leading-edge vortex pattern seen previously, but it is reversed. Instead, the flow separates at the trailing edge, with streamlines reattaching further forward along the wing chord, enveloping a coherent attached vortex (Fig. 3f, t_1). It is also distinct from previous descriptions of a starting vortex (sometimes referred to as a trailing-edge vortex) because it is both bound to the wing surface, rather than left in the wake, and makes a positive contribution to weight support. This transient trailing-edge vortex is quickly shed into the wake as the wing accelerates into the short translational phase, giving way to a leading-edge vortex (Fig. 3g) and a corresponding second peak in lift (Fig. 3, t_2).

A third peak in lift occurs owing to rapid supination during the onset of stroke reversal at the end of the downstroke (Fig. 3, t_3). The mechanism for this is the recently described phenomenon of rotational drag¹². The wing rotates initially around an axis close to the leading edge, resulting in strong forces normal to the posterior wing surface. The signature of this effect is that an intense negative pressure appears,

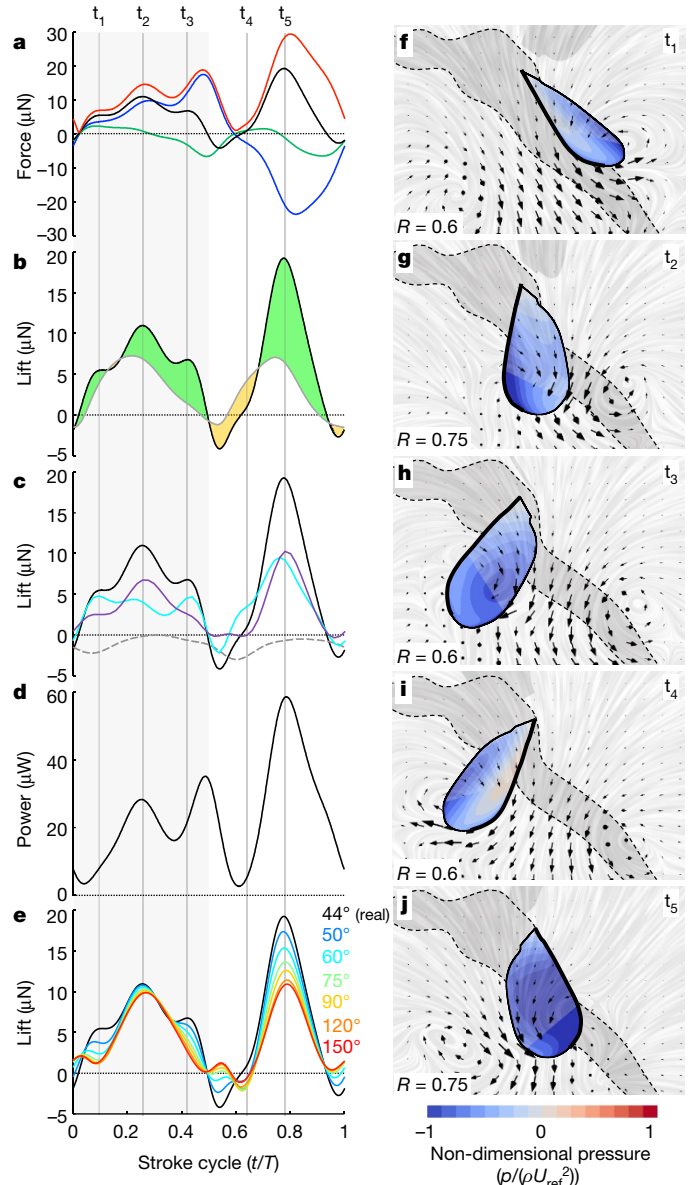


Figure 3 | Aerodynamic forces generated by wings and the mechanisms that produce them: trailing-edge vortices, leading-edge vortices and rotational drag. **a**, Single-wing total aerodynamic force (red), lift (black), drag (blue) and side-force (green). **b**, Lift from CFD (black) compared against a simple quasi-steady model (grey). Orange shading shows where the quasi-steady model over-predicts the force estimate from the CFD simulation, whereas green shows under-prediction. **c**, Partitioning of the lift force (black) into the portion derived from the integrated pressure on the anterior half of the wing (purple), the posterior half (cyan), and the viscous contribution (dashed). Note the fluctuating contributions during the downstroke ($t/T = 0$ – 0.5). **d**, Aerodynamic power. **e**, The effect of increasing wing stroke amplitude (see insert for range) while maintaining mean wing tip velocity is to reduce the relative contribution to lift attributable to unsteady effects. **f–j**, Surface pressure at t_1 – t_5 on the wing (blue to red shading). Overlain are instantaneous streamlines (grey) and flow velocity vectors (black arrows) for selected vertical slices through the three-dimensional flow field at planes $R = 0.6$ or $R = 0.75$ wing length from wing base. Body (dashed line) and wing outlines (solid line, leading edge in bold) are shown for orientation. ρ , density of air.

again, in the region of the trailing edge. We can differentiate between lift that is caused by rotational drag^{12,13} and rotational lift^{15,16} because the aerodynamic force vector is normal to the wing surface despite negligible translational velocity of the wing. As the wing decelerates (proportion through wingbeat, $t/T = 0.5$), rotational drag makes a

reduced contribution to weight support, becoming zero on the point of stroke reversal and even having a small negative value in some cases (Extended Data Fig. 8).

On the upstroke, the wing is inverted and the processes are repeated. As such, the fourth key instant (t4) corresponds to a new trailing-edge vortex (Fig. 3i) that quickly gives way to another leading-edge vortex (Fig. 3j). The peak in lift force during the late upstroke (t5) is a combination of the leading-edge vortex influence as the wing translates, and also rotational drag, because wing rotation begins earlier in the upstroke than the downstroke (Fig. 1c). The mechanisms are additive and it is notable that peak force generation happens this late in the wingbeat cycle. This contrasts with most other animals, with the exception of fruit flies^{17,18}, which exhibit maximal forces during the downstroke. High upstroke loads for mosquitoes will have consequences for the mechanical stresses on the wing, which may in turn predicate differences in anatomical architecture such as wing camber or vein cross-section profiles.

Quasi-steady modelling has been an important tool for aerodynamicists but it cannot encapsulate wake capture, rotational drag and nonlinear vortex phenomena. We produced a quasi-steady model that used dynamic force coefficients based on lift and drag polars at four Reynolds numbers (Extended Data Fig. 9) to highlight which wing-stroke forces are the result of unconventional mechanisms and are consequently poorly explained by a quasi-steady model. As expected, the key instants described above—in which extra lift is generated through rotational mechanisms—revealed a marked underestimate of the lift calculated from CFD simulations, with a further discrepancy noted as the lift due to rotational drag becomes negative at supination (Fig. 3b). To investigate further the relative importance of aerodynamic phenomena at wing rotation, we simulated the flow fields generated by larger amplitude wing strokes while maintaining the mean wing tip speed using CFD. This process shifts the balance of force generation back towards conventional, translational aerodynamics and diminishes the relative contribution of the rotational phases. The effect is demonstrated clearly by the increasing discrepancy at instances t1, t3 and t5 (Fig. 3e).

Leading-edge vortices on the up- and downstrokes produce large regions of negative pressure close to the leading edge of the wing (Fig. 3g, j); however, these are interleaved with trailing-edge vortices

and rotational drag effects that principally act on the posterior region, leading to chord-wise fluctuations in the centre of pressure. The key instants t1 (trailing-edge vortex), t3 (rotational drag) and t4 (upstroke trailing-edge vortex) show the dominance of the trailing portion of the wing in lift support, whereas t2 (the downstroke leading-edge vortex) shows the leading edge as dominant. In the case of t5, the leading-edge vortex during the upstroke has grown large enough to encroach into the aft portion of the wing and rotational drag is beginning to take effect, so the differential is negligible. Consequently, the wing undergoes fluctuations in the pitching torque, with the location of the centre of pressure sometimes acting in concert with the pitching of wing (Fig. 3c; for example, t1 and t4), resulting in a low power requirement that suggests passive pitching through aeroelastic effects (Fig. 3d).

Crucial to the ability of the mosquito to generate forces large enough to support its weight in flight is the high angular rate and exquisite timing of stroke reversal. Lift due to rotational drag is proportional to the square of the pitching angular rate, but equally important is the precise axis of rotation. In mosquitoes, the pitching rotational axis of the wing moves from leading to trailing edge during pronation at the end of the upstroke (Fig. 4a). By rotating first around an axis close to the leading edge, low pressure develops close to the trailing edge, creating a component of aerodynamic force that supports the weight of the mosquito and drawing the leading-edge vortex towards the trailing edge. If this rotational axis were maintained throughout pronation, the lift due to rotational drag would become negative as the wing angle passed through vertical. However, by shifting the axis of rotation progressively towards the trailing edge as the wing rotates, the new aerodynamic upper surface of the wing develops a region of negative pressure close to the leading edge. This region contributes positively to weight support through rotational drag at the start of the new half-stroke but also initiates flow separation for the new leading-edge vortex to form and grow during the downstroke (t2). At the end of the downstroke, the leading-edge vortex migrates towards the trailing edge and acts to initiate the trailing-edge vortex after supination. The trailing-edge vortex phenomenon is a wake capture event during stroke reversal—when the wing is translating slowly—so the mechanical work performed by the flight motor is very low, and lift efficiency is consequently relatively high at this instant (Fig. 3d, t1). Immediately after the wing passes through the vertical alignment, the aerodynamic torque

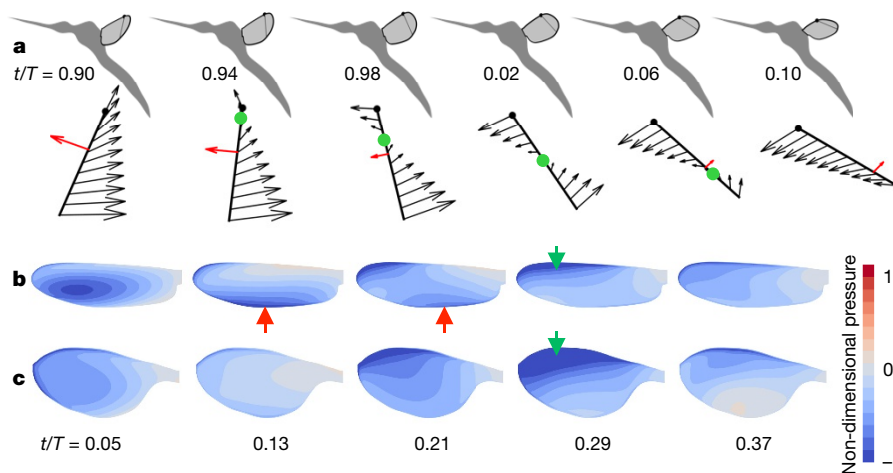


Figure 4 | Wing pronation. **a**, The end of each half-stroke in mosquitoes is characterized by a shift in the rotational axis (green dot) from leading to trailing edge. Black arrows indicate local motion of the wing during pronation (at $R = 0.75$ wing length, indicated in top row); red arrows indicate the resultant aerodynamic force vector (depicted at the chord-wise centre of pressure). Despite rapid pitching down at $t/T = 0.10$ and faster motion of the leading edge, the trailing edge remains almost stationary yet generates the majority of the lift at this instant owing to the formation of a trailing-edge vortex caused by the induced flow from the

preceding upstroke. **b**, **c**, Pressure distributions (shaded blue to red) on the upper surface of the mosquito (**b**) and fruit fly (**c**) at five moments through the downstroke. Red arrows in **b** show the signature of the trailing-edge vortex, visualized by a region of intense low pressure along the trailing portion of the wing, which is not present on the fruit fly wing (**c**). Later in the downstroke, a low-pressure region from the leading-edge vortex starts outboard and grows towards the wing root, as described elsewhere²⁴ for both species (green arrow).

on the wing provided by the captured trailing-edge vortex acts to pitch the wing passively in preparation for the next sweep.

The great benefit of lift mediated by rotational drag is that the aerodynamic force (in contrast to conventional lift from a sweeping wing) is independent of radial position. It is therefore equally effective along the entire wingspan, even in the portion of the wing close to the root where velocity caused by the sweep of the wing—and hence lift caused by translation—is near zero. This feature, in combination with reduced inertial costs during rotation and smaller pitching torques due to reduced moment arm length, is probably a key factor in shaping the high aspect ratio wings of mosquitoes. We do not necessarily expect these aerodynamic features to be unique to mosquitoes, but the trailing-edge vortex wake capture mechanism is not a notable feature of fruit fly flight, despite operating at similar Reynolds numbers (Fig. 4b, c). It remains an open question as to why mosquitoes have evolved to operate far outside the usual bounds of kinematic patterns used by other insects. Given that high-frequency flapping will undoubtedly incur greater inertial power requirements, one can presume compensatory selective advantages, perhaps in the domain of acoustic communication¹⁹.

Online Content Methods, along with any additional Extended Data display items and Source Data, are available in the online version of the paper; references unique to these sections appear only in the online paper.

Received 21 October 2016; accepted 27 February 2017.

Published online 29 March; corrected online 5 April 2017

(see full-text HTML version for details).

- Simões, P. M. V., Ingham, R. A., Gibson, G. & Russell, I. J. A role for acoustic distortion in novel rapid frequency modulation behaviour in free-flying male mosquitoes. *J. Exp. Biol.* **219**, 2039–2047 (2016).
- Chin, D. D. & Lentink, D. Flapping wing aerodynamics: from insects to vertebrates. *J. Exp. Biol.* **219**, 920–932 (2016).
- Ellington, C. P., van den Berg, C., Willmott, A. P. & Thomas, A. L. R. Leading-edge vortices in insect flight. *Nature* **384**, 626–630 (1996).
- Somps, C. & Luttges, M. Dragonfly flight: novel uses of unsteady separated flows. *Science* **228**, 1326–1329 (1985).
- Bomphrey, R. J., Srygley, R. B., Taylor, G. K., Nudds, R. L. & Thomas, A. L. R. Visualising the flow around insect wings. *Phys. Fluids* **14**, S4 (2002).
- Thomas, A. L. R., Taylor, G. K., Srygley, R. B., Nudds, R. L. & Bomphrey, R. J. Dragonfly flight: free-flight and tethered flow visualizations reveal a diverse array of unsteady lift-generating mechanisms, controlled primarily via angle of attack. *J. Exp. Biol.* **207**, 4299–4323 (2004).
- Bomphrey, R. J., Taylor, G. K. & Thomas, A. L. R. Smoke visualization of free-flying bumblebees indicates independent leading-edge vortices on each wing pair. *Exp. Fluids* **46**, 811–821 (2009).
- Srygley, R. B. & Thomas, A. L. R. Unconventional lift-generating mechanisms in free-flying butterflies. *Nature* **420**, 660–664 (2002).
- Videler, J. J., Stamhuis, E. J. & Povel, G. D. E. Leading-edge vortex lifts swifts. *Science* **306**, 1960–1962 (2004).
- Warrick, D. R., Tobalske, B. W. & Powers, D. R. Aerodynamics of the hovering hummingbird. *Nature* **435**, 1094–1097 (2005).
- Hedenström, A. *et al.* Bat flight generates complex aerodynamic tracks. *Science* **316**, 894–897 (2007).
- Nakata, T., Liu, H. & Bomphrey, R. J. A CFD-informed quasi-steady model of flapping wing aerodynamics. *J. Fluid Mech.* **783**, 323–343 (2015).
- Whitney, J. P. & Wood, R. J. Aeromechanics of passive rotation in flapping flight. *J. Fluid Mech.* **660**, 197–220 (2010).
- Ellington, C. P. The aerodynamics of hovering insect flight. VA vortex theory. *Phil. Trans. R. Soc. Lond. B* **305**, 115–144 (1984).
- Dickinson, M. H., Lehmann, F.-O. & Sane, S. P. Wing rotation and the aerodynamic basis of insect flight. *Science* **284**, 1954–1960 (1999).
- Sane, S. P. & Dickinson, M. H. The aerodynamic effects of wing rotation and a revised quasi-steady model of flapping flight. *J. Exp. Biol.* **205**, 1087–1096 (2002).
- Aono, H., Liang, F. & Liu, H. Near- and far-field aerodynamics in insect hovering flight: an integrated computational study. *J. Exp. Biol.* **211**, 239–257 (2008).
- Fry, S. N., Sayaman, R. & Dickinson, M. H. The aerodynamics of hovering flight in *Drosophila*. *J. Exp. Biol.* **208**, 2303–2318 (2005).
- Cator, L. J., Arthur, B. J., Harrington, L. C. & Hoy, R. R. Harmonic convergence in the love songs of the dengue vector mosquito. *Science* **323**, 1077–1079 (2009).
- Altschuler, D. L., Dickson, W. B., Vance, J. T., Roberts, S. P. & Dickinson, M. H. Short-amplitude high-frequency wing strokes determine the aerodynamics of honeybee flight. *Proc. Natl Acad. Sci. USA* **102**, 18213–18218 (2005).
- Willmott, A. P. & Ellington, C. P. The mechanics of flight in the hawkmoth *Manduca sexta*. I. Kinematics of hovering and forward flight. *J. Exp. Biol.* **200**, 2705–2722 (1997).
- Liu, H. Integrated modeling of insect flight: From morphology, kinematics to aerodynamics. *J. Comput. Phys.* **228**, 439–459 (2009).
- Vance, J. T. & Roberts, S. P. The effects of artificial wing wear on the flight capacity of the honey bee *Apis mellifera*. *J. Insect Physiol.* **65**, 27–36 (2014).
- Phillips, N., Knowles, K. & Bomphrey, R. J. The effect of aspect ratio on the leading-edge vortex over an insect-like flapping wing. *Bioinspir. Biomim.* **10**, 056020 (2015).

Supplementary Information is available in the online version of the paper.

Acknowledgements The authors were supported by the EPSRC (EP/H004025/1 and EP/M003698/1), BBSRC (BB/J001244/1). R.J.B. was supported by an EPSRC Career Acceleration Fellowship. S.M.W. was supported by a Royal Society University Research Fellowship. The work reported in this paper was funded by the Autonomous Systems Underpinning Research (ASUR) programme under the auspices of the Defence Science and Technology Laboratory (Dstl), UK Ministry of Defence. The authors acknowledge useful discussions with I. Russell and G. Gibson, P. Simoes for rearing the mosquitoes, and F. Albert-Davie and M. Inglis for assistance during raw data collection. The authors thank G. Taylor for the loan of four high-speed cameras purchased on European Research Council (ERC) grant 204513, and H. Liu for the permission to use the simulator and surface pressure distribution of the fruit fly wing.

Author Contributions R.J.B. and S.M.W. conceived the experimental design; N.P. and S.M.W. designed and constructed the apparatus and N.P. led the data collection; all authors contributed to data collection; S.M.W. processed the raw data to extract detailed kinematics; T.N. performed the CFD simulations; N.P., T.N. and R.J.B. collected and processed the PIV data; R.J.B. drafted the manuscript; all authors contributed to data interpretation and manuscript preparation.

Author Information Reprints and permissions information is available at www.nature.com/reprints. The authors declare no competing financial interests. Readers are welcome to comment on the online version of the paper. Publisher's note: Springer Nature remains neutral with regard to jurisdictional claims in published maps and institutional affiliations. Correspondence and requests for materials should be addressed to R.J.B. (rbomphrey@rvc.ac.uk).

Reviewer Information *Nature* thanks S. Swartz and the other anonymous reviewer(s) for their contribution to the peer review of this work.

METHODS

Data reporting. No statistical methods were used to predetermine sample size. The experiments were not randomized and the investigators were not blinded to allocation during experiments and outcome assessment.

Mosquitoes. *Culex quinquefasciatus* 'Muheza' strain, originally sourced from the London School of Hygiene and Tropical Medicine, were bred at the University of Sussex and tested at the Royal Veterinary College, London. Groups were maintained in microclimate chambers with controlled humidity (70–75%), temperature ($26 \pm 2^\circ\text{C}$) and 12:12 h light cycles. Males between 4 and 14 days post-emergence were tested in groups of four to eight individuals.

Kinematics acquisition. Mosquito wing kinematics were measured using the apparatus illustrated in Extended Data Fig. 1a, b, comprised of eight high-speed cameras (Photron SA3: 384×352 pixels, Photron Europe, Ltd) operating at 10,000 frames per second with an exposure time of $5 \mu\text{s}$. Each camera was fitted with a 180 mm macro lenses with aperture set at $f/16$. Consistent backlighting for each camera was provided by a co-axial, high-power infrared LED with divergent and Fresnel lenses to collimate the light in paths of approximately 25 mm diameter. The cameras were arranged such that they viewed a common volume of approximately $20 \times 20 \times 20$ mm at the centre of a transparent flight arena measuring $330 \times 330 \times 230$ mm. In total, we processed 425 wingbeats, over 15 sequences from between 12 and 15 individuals, discernible by their wing length (Extended Data Fig. 1c).

Kinematics reconstruction. The eight cameras were calibrated using custom-written, bundle adjustment software running in Matlab (The Mathworks Inc.), which provides estimates of the intrinsic and extrinsic camera parameters, while simultaneously calculating the spatial coordinates of points on a 2D calibration grid in a series of positions and orientations²⁵.

We selected 15 sequences for kinematic analysis (Extended Data Fig. 1d), which included all sequences where both wings were visible in seven or more camera views for a minimum of eight wingbeats. Four points on the body were manually registered in three camera views; the base of the proboscis, the tip of the abdomen, and the left and right wing roots. These points were used to calculate the 3D position and orientation of the mosquito body for each frame. A fully automated shape-carving method was used to reconstruct the coordinates of the wing outline²⁶. The wing outline was first identified in each camera view using standard image-processing tools in Matlab (Fig. 1b). The shape-carving algorithm then identified voxels corresponding to the wing outlines when projected onto each camera plane.

The wing tip position was determined by identifying the voxels along the wing outline that were furthest from the wing root. Voxels corresponding to the leading and trailing edges of the wing were then separated using k -means clustering and a cubic spline was fitted to each edge from the wing base to the wing tip. The span-wise variation in pitch angle, α , was summarized by regressing the angle between the leading and trailing edge of the wing against span-wise distance along the wing, to give a pitch offset and linear twist gradient.

Computational fluid dynamics (CFD). The morphological model for CFD analyses was constructed by digitizing the wing outline from microscope images of excised wings and fitting ellipses to the body in the raw video images. Assuming a low leakiness of hairs at the anterior margin due to the ultra-low Reynolds number²⁷, we used outlines incorporating the hairs as part of the wing shape. The mean shape of three individuals (Extended Data Fig. 10a; red lines) was used for the surface mesh (Extended Data Fig. 10b). Uniform thickness was assumed to be 1% of mean chord length with elliptic smoothing at the leading and trailing edges as well as the wing tip and base. The body surface was extracted by manually fitting a series of ellipses to the body in each camera view. Each ellipse was normal to the central axis of the body, which was determined separately using the positions of head and body landmarks. The ellipses were then interpolated by cubic splines and used to generate the mesh surface shown in Extended Data Fig. 10c, d.

For our CFD model, we used a dynamic flight simulator^{22,28} that is based on the incompressible, unsteady three-dimensional Navier–Stokes equations and can easily integrate the realistic morphology, kinematics and aerodynamics of insect flight. The simulator utilizes a multi-block, overset-grid method in which the computational domain is decomposed into the local grid, clustered near the wings and body, and a global Cartesian grid. The wing and body grids in Extended Data Fig. 10e were generated from the surface mesh. The minimum grid spacing from surface is defined on the basis of $0.1/\sqrt{\text{Re}}$ (Re = Reynolds number). The distance between the surface and outer boundary is set to be $2.0 c_m$ (mean chord lengths) for wing and $1.0 c_m$ for body grids. The outer boundary conditions for local grids are given by a Cartesian background grid ($28R \times 14R \times 28R$; Extended Data Fig. 10f). We assumed a symmetric motion of the left and right wings, and applied a symmetric boundary condition at the sagittal plane of the body and background grid. The wing grid was regenerated every time-step after twisting the wing surface,

and rotated around wing base. The flapping angles were interpolated by a fifth order Fourier series.

Self-consistency was tested by four CFD cases with coarse, fine and finer grids, and a reduced time-step interval, Δt . The time-series data of vertical force, mean aerodynamic force and power are summarized in Extended Data Fig. 10g. Although there is a slight difference in the coarse case, there is no large discrepancy observed among the other cases. Two time steps (comparing fine and finer Δt) also show little difference. Therefore, the grids for fine case with $\Delta t = 0.01$ was used for all subsequent simulations.

Particle image velocimetry (PIV). Mosquitoes were placed in the centre of a clear tank ($380 \times 140 \times 300$ mm) by a thin wire attached to the dorsal side of the thorax using cyanoacrylate glue. The tank was seeded with a mist of olive oil droplets of approximately $1 \mu\text{m}$ diameter, generated by a compressed air seeding generator (LaVision UK, Ltd), and the flow was left for a few minutes to become quiescent. The seeding particles were illuminated using a 10 mJ dual-cavity pulsed laser (Litron LDY-301PIV, ND: YLF, 527 nm, Litron Lasers, Ltd). The beam diverged into a sheet of approximately 1 mm thickness after passing through a 20 mm cylindrical lens, entering the flight arena from above such that the sheet was parallel with the sagittal plane of the mosquito, incident with the wing half way from root to tip ($R = 0.5$ wing length). Images were captured over a sampling area of 17×17 mm around the wing using a single high-speed camera (Photron SA3: 2,000 frames per second, $1,024 \times 1,024$ pixels, Photron Europe, Ltd) fitted with a 180 mm macro lens (Tamron) whose axis was normal to the light sheet.

The camera and laser were driven using DAVIS v.7.2.2 software and synchronized by a high-speed controller (LaVision UK, Ltd) operating at a rate of 1,000 image pairs per second. The system was post-triggered by a TTL (transistor-transistor logic) signal and each recording captured 1,361 image pairs (limited by camera buffer capacity). The camera was calibrated using a custom calibration plate (circle diameter $\phi = 1$ mm; circle separation $\Delta x = 2$ mm) and the calibration procedure in Davis v.7.2.2 (LaVision UK, Ltd).

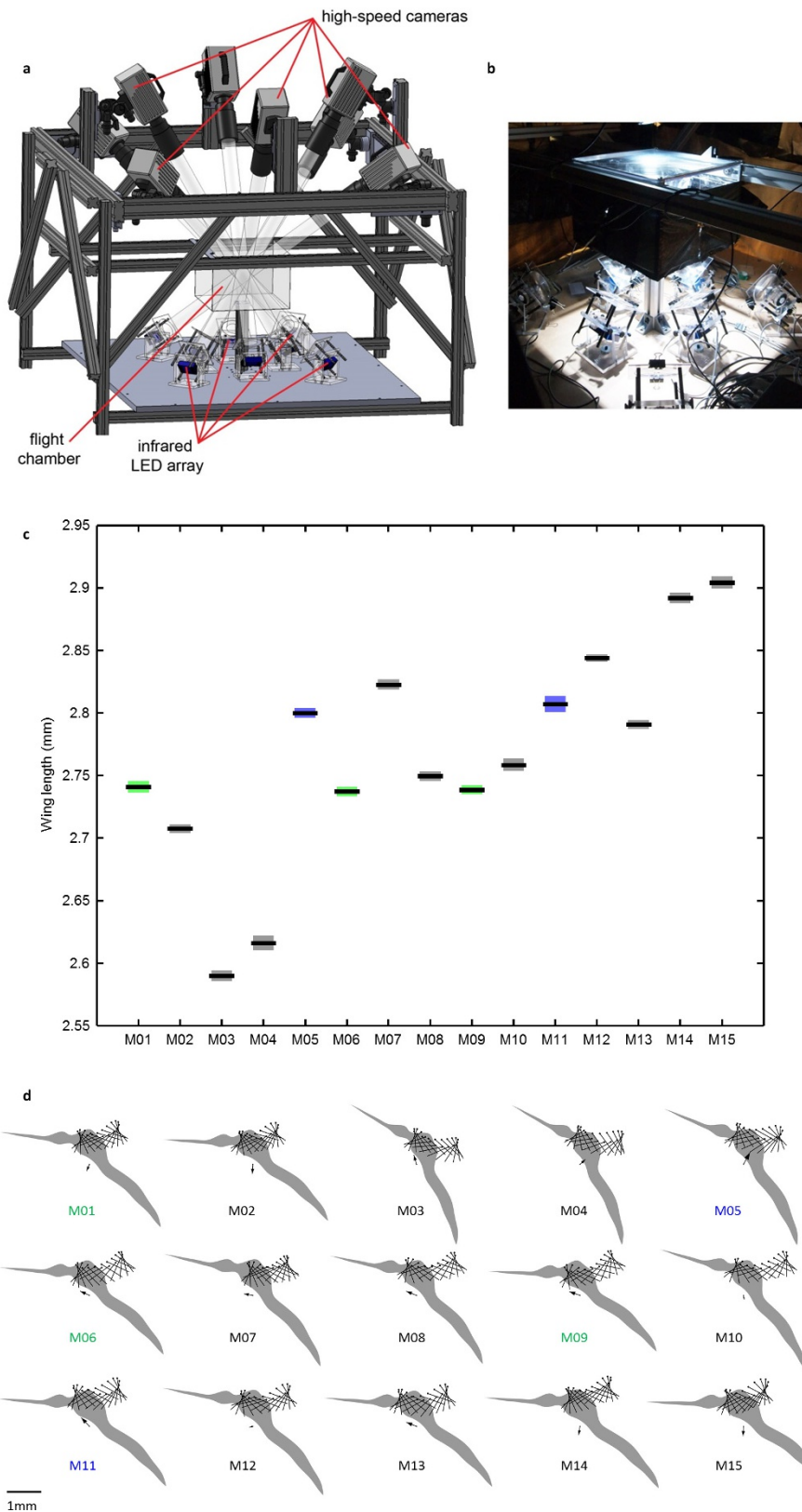
Raw images were pre-processed by subtraction of a sliding background (2 pixels) and particle intensity normalization (min/max filter, 10 pixels) to remove any stationary elements in the images (for example, reflection from body, legs and antenna). The reflection from the wing is masked manually for presentation. After filtering, the images were cross-correlated to calculate fluid vector fields by multi-path correlation with a decreasing interrogation window size from 64×64 (50% overlap) to 16×16 (50% overlap). PIV calculations were performed using Davis v.8.1.5 (LaVision UK, Ltd). Post processing of vector fields involved filling up of empty spaces by interpolation and a 3×3 smoothing. We selected the frames before the mosquito began to respond to the laser light (approximately the first 50 frames in a sequence) with relatively low glare on wing.

Blade element model with quasi-steady assumption. In order to highlight the unconventional aerodynamics of hovering mosquitoes, we compared the forces from the CFD simulations with a blade element model with the quasi-steady assumption that takes into account the translational circulation and drag, and added mass^{12,29}. The lift and drag force coefficients, C_L and C_D , were calculated using the mean lift and drag from a separate CFD analysis that simulates a spinning mosquito wing model. We used the 3rd cycle ($1,080^\circ$ – $1,170^\circ$) to account for the effect of induced downwash from previous strokes. As we found a strong dependency of force coefficients profile on Reynolds number (50–300), C_L and C_D in the blade element model were interpolated by a 2D spline, assuming those as the functions of angle of attack and instantaneous Reynolds number on the basis of mean chord length and instantaneous wing tip velocity. The range of Reynolds number for C_L and C_D covers the maximum instantaneous Reynolds number of *Culex* mosquitoes, 250, and the C_L and C_D at $\text{Re} = 50$ (the 20th percentile of instantaneous Reynolds number) was used if the instantaneous Reynolds number dropped to a value lower than 50.

Data availability. Data sets underpinning the current study are available in the Dryad repository at <http://dx.doi.org/10.5061/dryad.tc29h>.

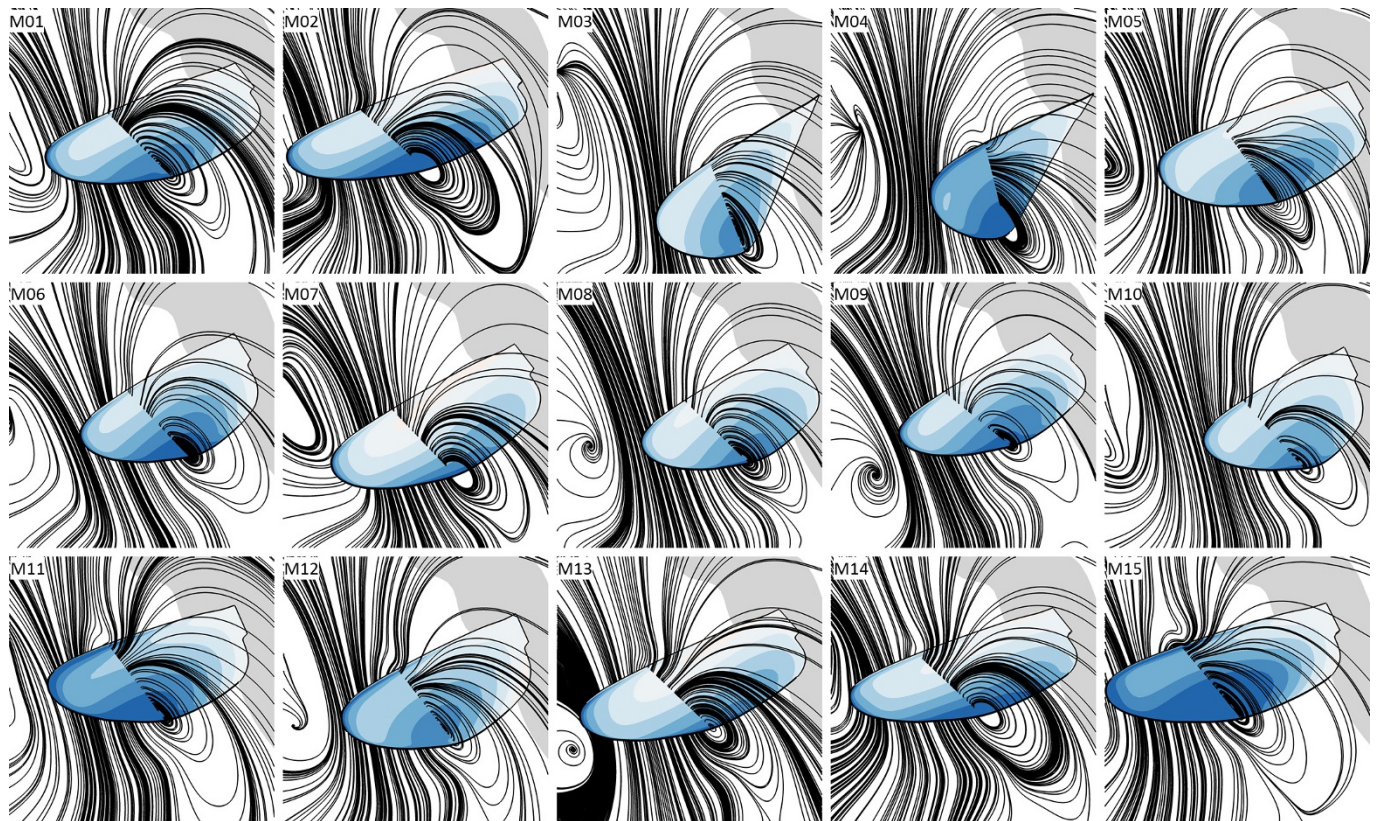
Code availability. The CFD solver²² and kinematics acquisition code^{25,26} are described in further detail elsewhere.

25. Walker, S. M., Thomas, A. L. R. & Taylor, G. K. Photogrammetric reconstruction of high-resolution surface topographies and deformable wing kinematics of tethered locusts and free-flying hoverflies. *J. R. Soc. Interface* <http://dx.doi.org/10.1098/rsif.2008.0245> (2009).
26. Walker, S. M., Thomas, A. L. R. & Taylor, G. K. Operation of the alula as an indicator of gear change in hoverflies. *J. R. Soc. Interface* <http://dx.doi.org/10.1098/rsif.2011.0617> (2011).
27. Cheer, A. Y. L. & Koehl, M. A. R. Paddles and rakes: fluid-flow through bristled appendages of small organisms. *J. Theor. Biol.* **129**, 17–39 (1987).
28. Nakata, T. & Liu, H. A fluid-structure interaction model of insect flight with flexible wings. *J. Comput. Phys.* **231**, 1822–1847 (2012).
29. Berman, G. J. & Wang, Z. J. Energy-minimizing kinematics in hovering insect flight. *J. Fluid Mech.* **582**, 153–168 (2007).



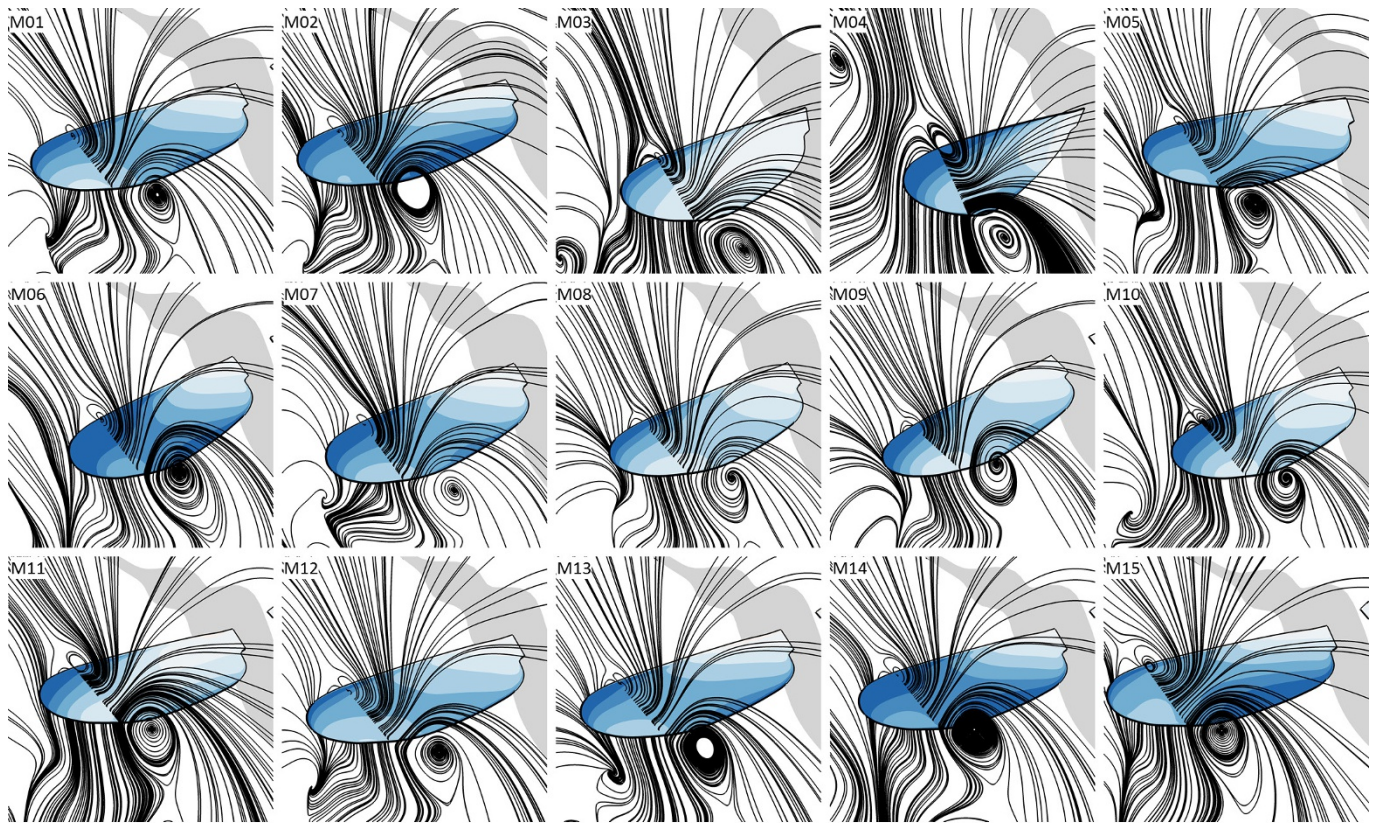
Extended Data Figure 1 | Mosquito kinematics acquisition rig, wing lengths and mean kinematic patterns. **a**, **b**, CAD representation (**a**) and photograph of the apparatus (**b**) used to record the body motion and wing kinematics of mosquitoes. The recording volume lies at the intersection of the fields of view of eight high-speed cameras, each creating a silhouette image of the mosquito by the shadow from high power IR-LED illumination. **c**, Wing-length estimates for mosquitoes captured in each of 15 sequences (M01-M15). Each estimate shows the median as a black line with shading representing the 95% confidence

interval based upon all wingbeats from each sequence. Green and blue boxes group sequences that could not be reliably separated using Tukey's honestly significant difference criterion, although they may come from different individuals of very similar size. As such, our fully processed data set of 15 sequences comprises between 12 and 15 individual mosquitoes. **d**, Mean wingbeat kinematics for all wingbeats in each of 15 recorded sequences. With reference to **c**, M01, M06 and M09, coloured green, may be from the same individual. Similarly, M05 and M11, coloured blue, may also be from a single individual.



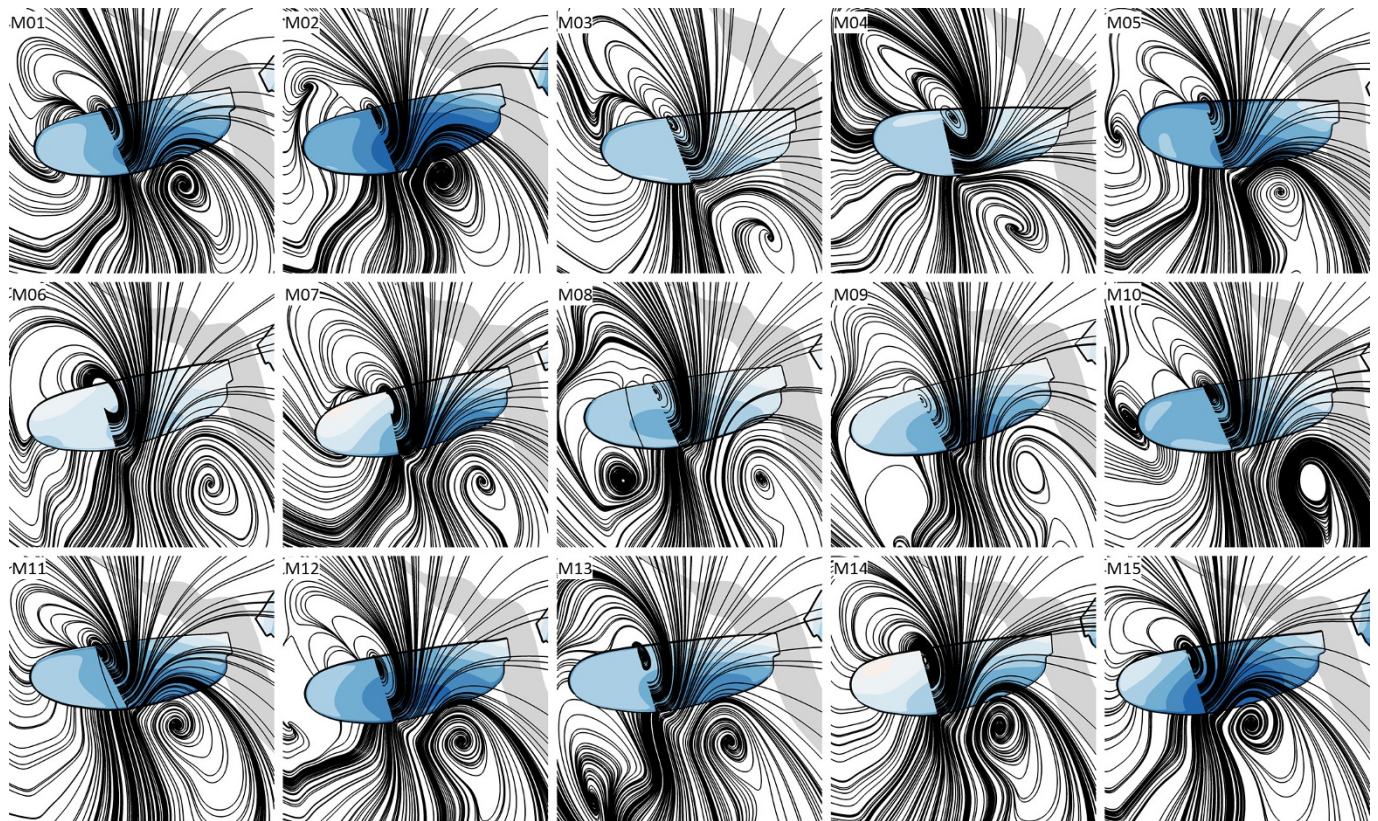
t1. Trailing edge vortex (downstroke)

Extended Data Figure 2 | Wing surface pressure distribution and fluid flow visualized by streamlines showing consistency across each of the 15 mosquito sequences. Each image corresponds to key instant t1. Formation of the trailing-edge vortex owing to capture of the induced flow from the preceding upstroke causes a distinct region of low pressure on the posterior portion of the wing.



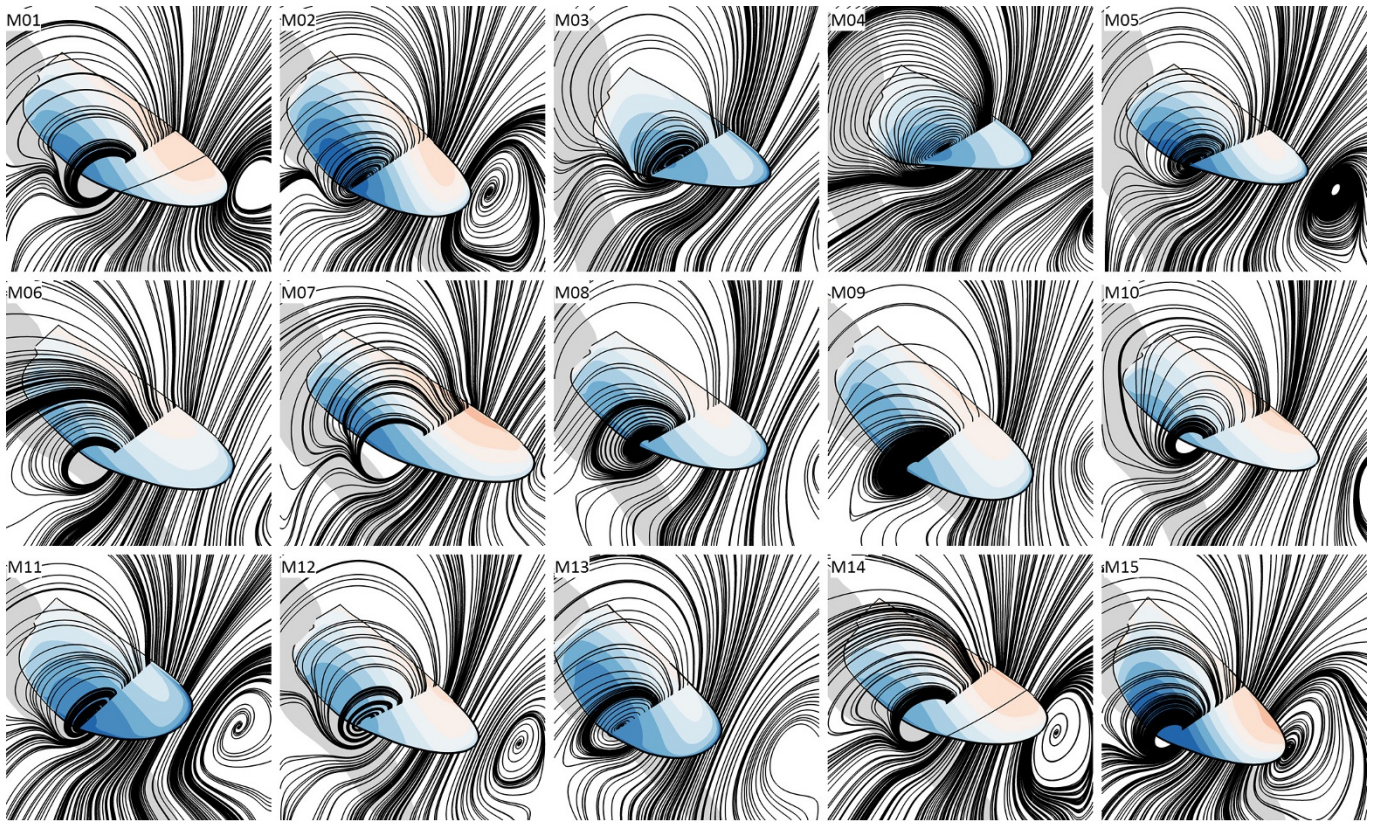
t2. Leading-edge vortex (downstroke)

Extended Data Figure 3 | Wing surface pressure distribution and fluid flow visualized by streamlines showing consistency across each of the 15 mosquito sequences. Each image corresponds to key instant t2. The downstroke force peak is dominated by a leading-edge vortex and corresponding low pressure on the anterior portion of the wing. The trailing-edge vortex has usually shed by this point in the stroke cycle.



t3. Rotational drag (supination)

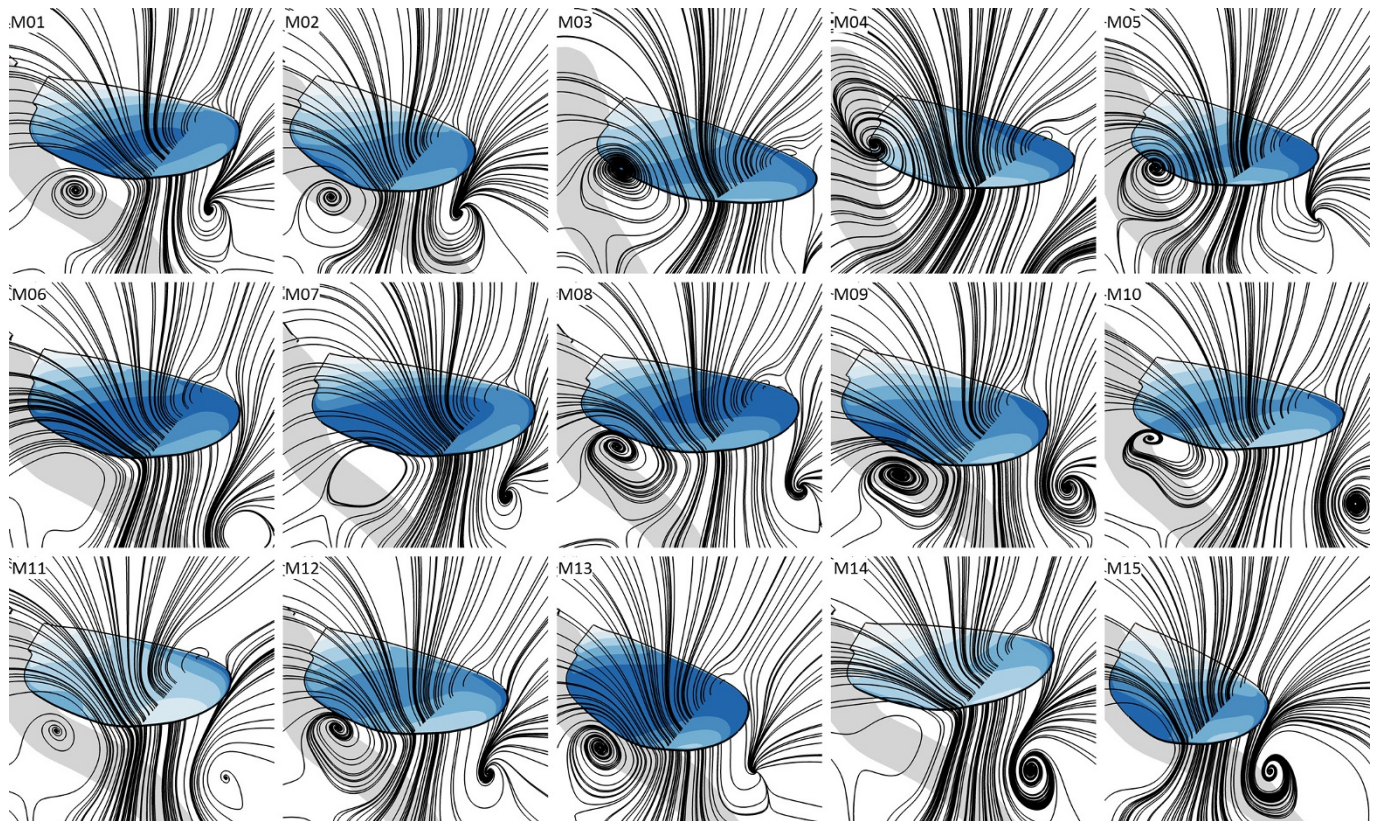
Extended Data Figure 4 | Wing surface pressure distribution and fluid flow visualized by streamlines showing consistency across each of the 15 mosquito sequences. Each image corresponds to key instant t3. A low-pressure region is evident on the posterior portion of the wing caused by lift from rotational drag as the wing rotates around an axis close to the leading edge.



t4. Trailing-edge vortex (upstroke)

Extended Data Figure 5 | Wing surface pressure distribution and fluid flow visualized by streamlines showing consistency across each of the 15 mosquito sequences. Each image corresponds to key instant t4. Formation of a trailing-edge vortex on the aerodynamic

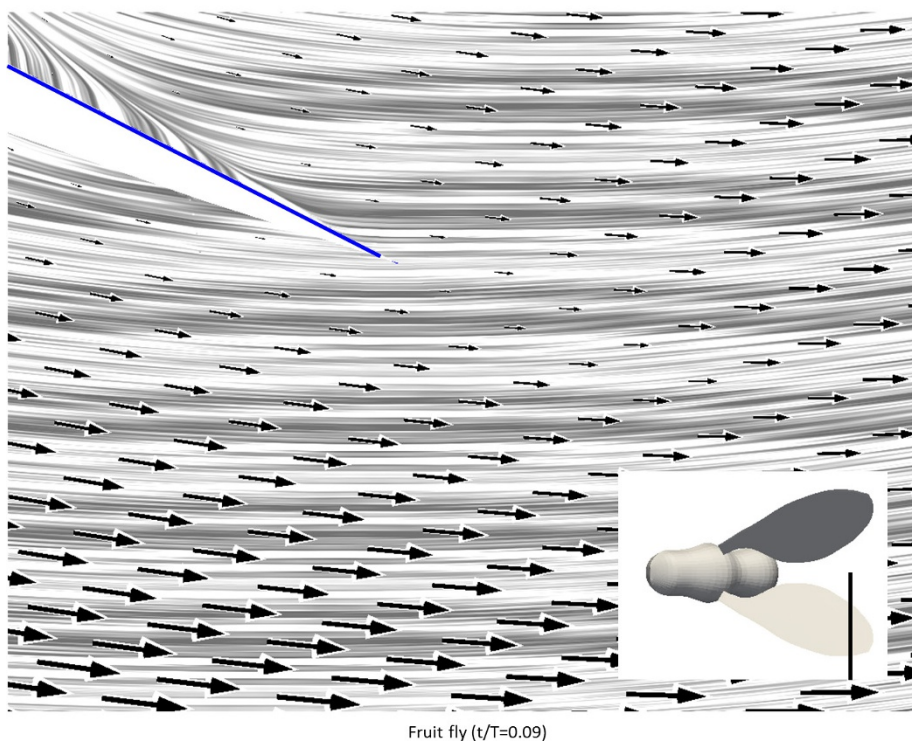
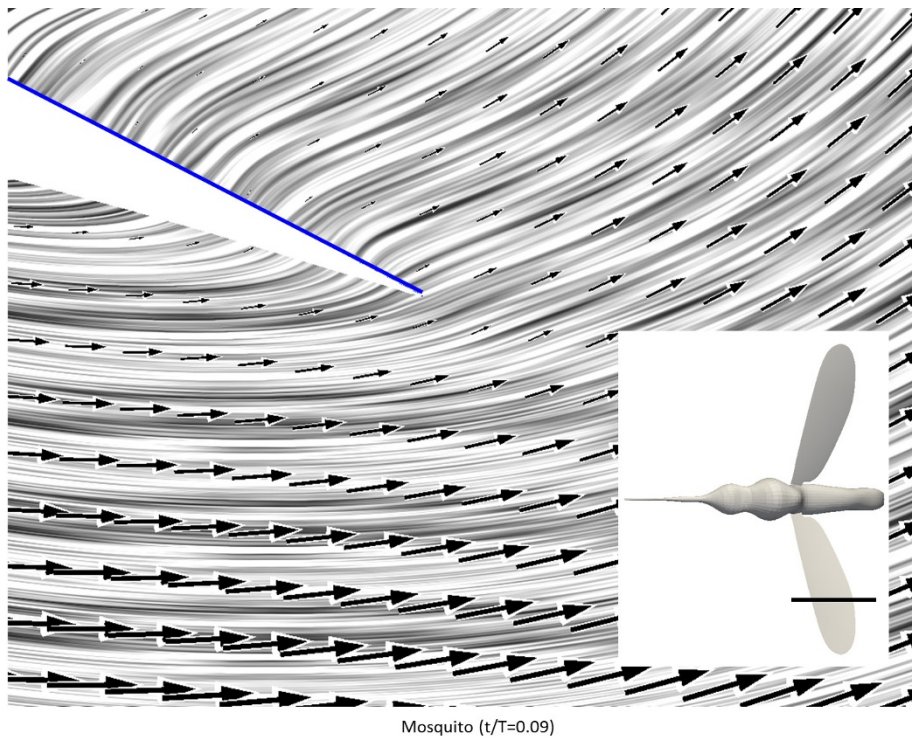
upper, (anatomical ventral) surface of the wing during the upstroke due to capture of the induced flow from the preceding downstroke causes a distinct region of low pressure on the posterior portion of the wing.



t5. Leading-edge vortex and rotational drag (upstroke)

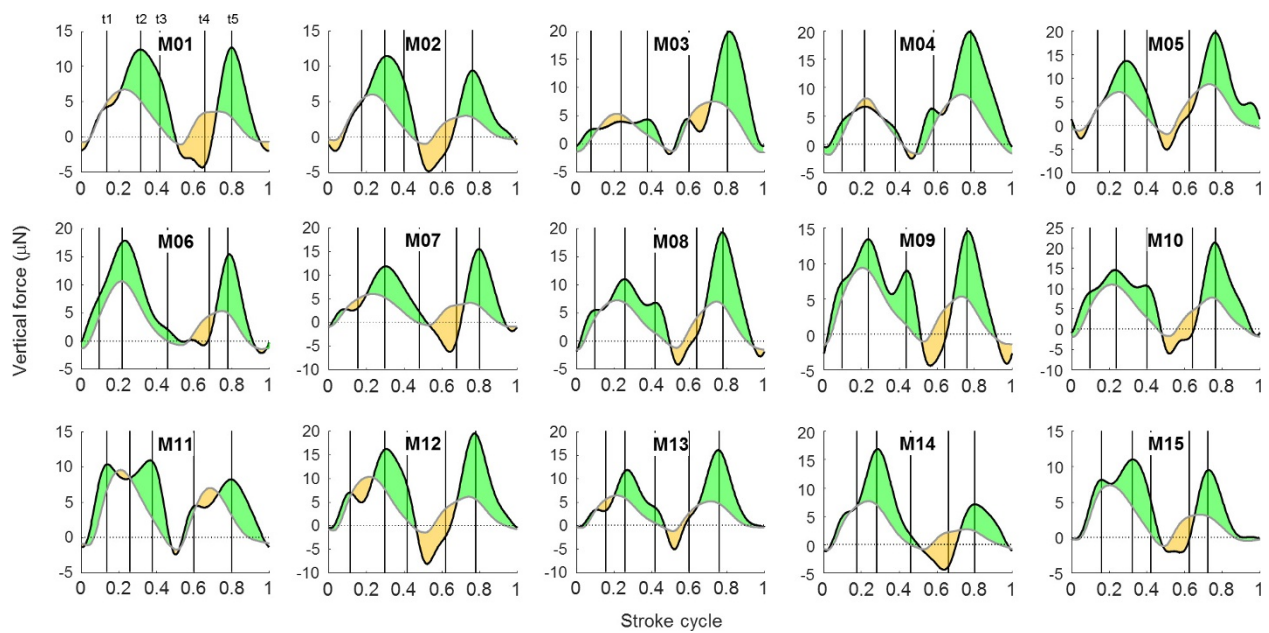
Extended Data Figure 6 | Wing surface pressure distribution and fluid flow visualized by streamlines showing consistency across each of the 15 mosquito sequences. Each image corresponds to key instant t5. A low-pressure region exists over much of the aerodynamic upper, (anatomical ventral) surface of the wing as the result of a combination

of rotational drag (caused by wing rotation around an axis close to the leading edge) and the remnants of the leading-edge vortex of the upstroke (which is no longer coherent in most examples but is retained in M03, M04, M06, M08, M11).

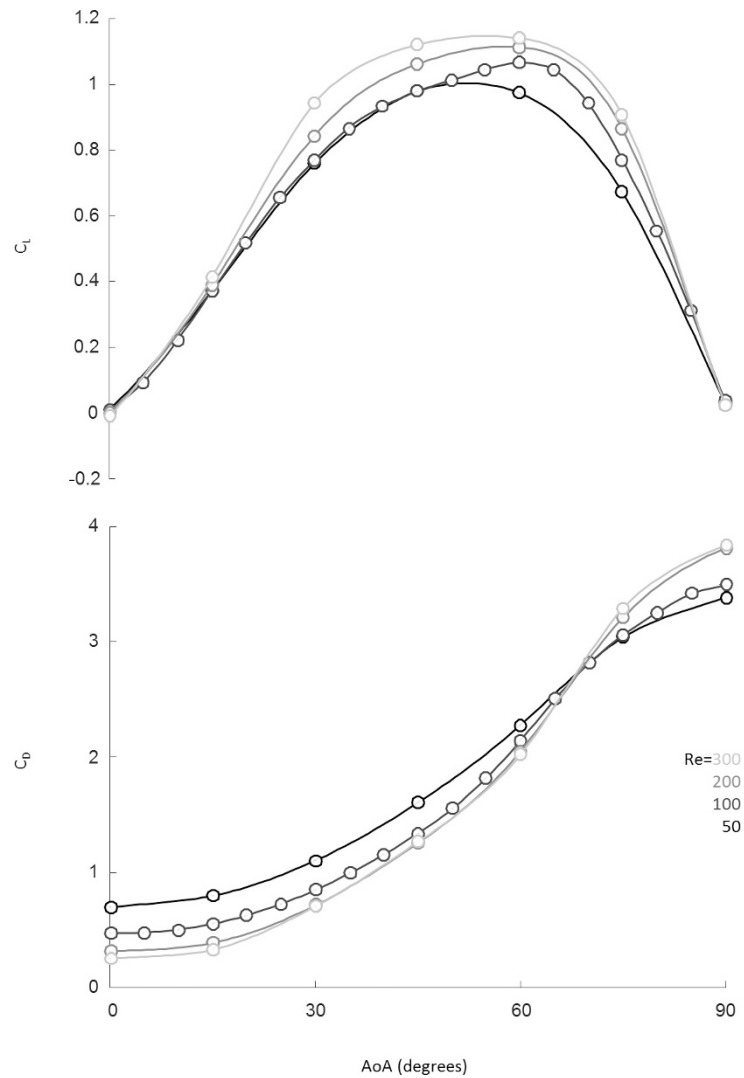


Extended Data Figure 7 | Comparison of the local flow conditions at the trailing edge of the wings of mosquitoes and fruit flies during pronation ($t/T = 0.09$). The comparatively higher local angle of attack of the mosquito wing is caused by the induced flow from the preceding upstroke. This is a product of kinematic tuning and a form of wake

capture that leads to roll up of a transient, coherent, trailing-edge vortex. The vortex contributes to weight support along much of the length of the slender mosquito wing, despite it having little ground velocity during the rotational phase of the stroke cycle.

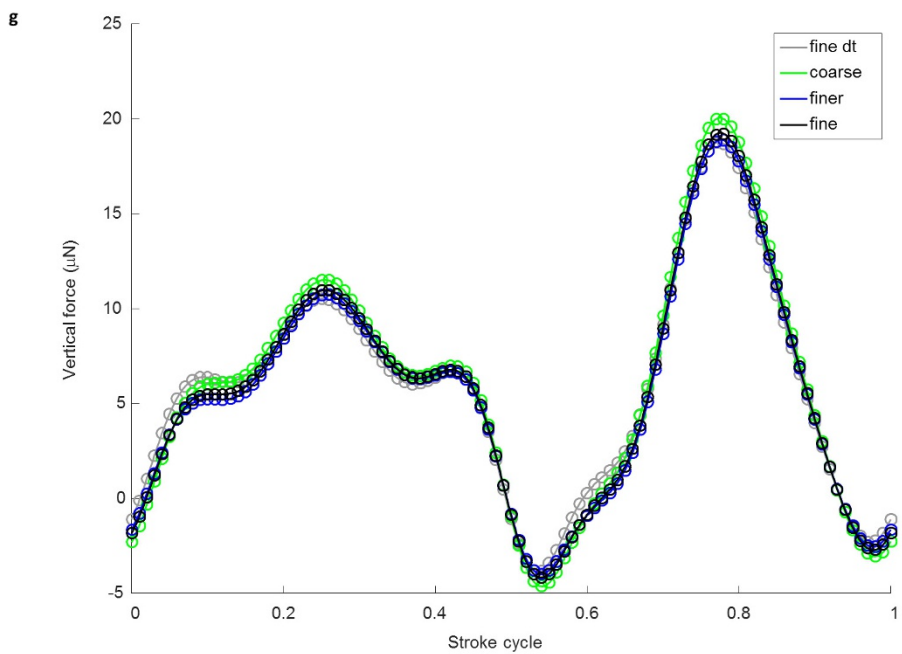
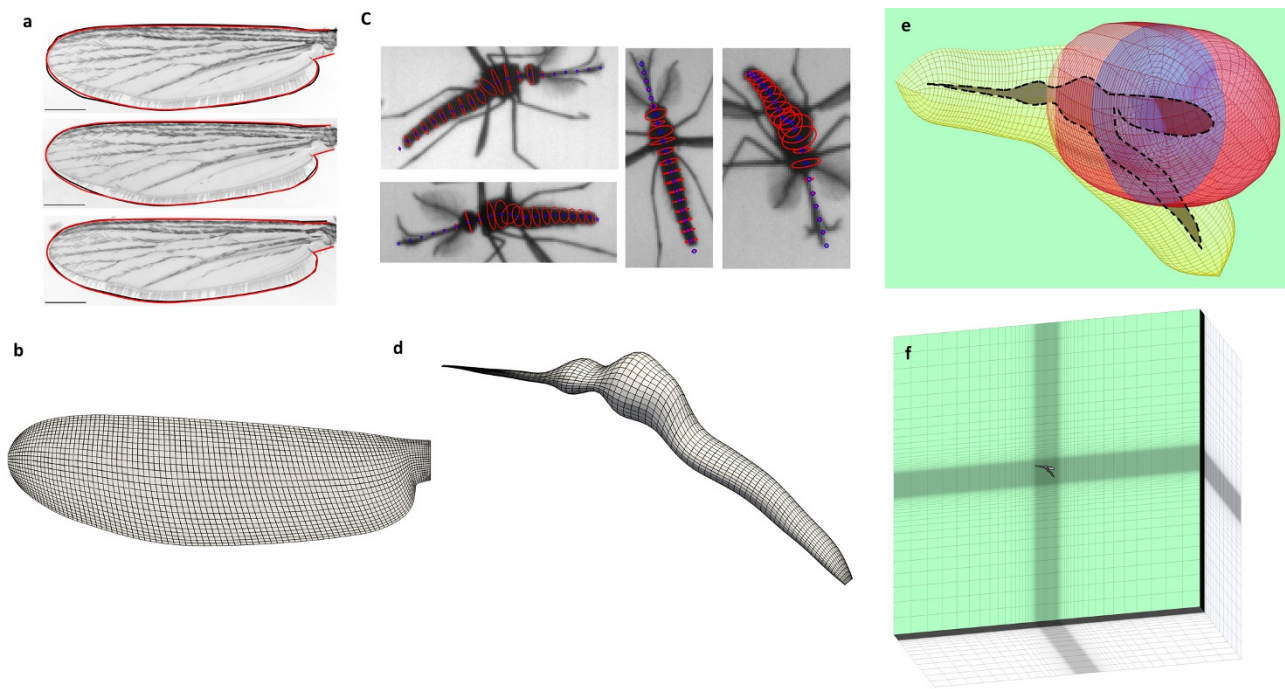


Extended Data Figure 8 | Comparison of computed CFD lift force (black) compared against a simple quasi-steady model (grey) for each of 15 mosquito flight sequences. Orange shading shows where the quasi-steady model over-predicts the force estimate from the CFD simulation, whereas green shows under-prediction. (See also Fig. 3)



Extended Data Figure 9 | Lift and drag polars from high-fidelity CFD simulations of the mosquito wing model in continuous rotational sweep at four Reynolds numbers. These were used to create dynamic lift coefficients for the blade element modelling with quasi-steady assumption.

Coefficients are calculated for the third rotation, to account for the reduction in effective angle of attack when wings operate in the induced downwash from the preceding wing stroke.



	grid (wing)	grid (body)	grid (background)	time step	Mean vertical force (mN)	Mean aerodynamic power (mW)
finer	71x121x51	41x111x31	188x108x201	0.01	5.69 (-1.95)	22.72 (-2.25)
fine	51x101x41	33x91x21	141x81x151	0.01	5.80 (0.00)	23.24 (0.00)
coarse	31x81x31	21x71x15	94x54x101	0.01	6.06 (4.47)	24.46 (5.25)
fine dt	51x101x41	33x91x21	141x81x151	0.005	5.91 (1.79)	22.99 (-1.10)

Extended Data Figure 10 | Morphology extraction and the CFD grid used for simulations. **a, b**, We used the mean wing planform of three mosquitoes, extracted from microscope images of recently excised wings, to generate the wing grids used in our CFD simulations. **c, d**, The body shape was approximated from the silhouettes in the raw video data by

fitting ellipses normal to the central axis of the body taken from each of the eight camera views. **e, f**, Local and background grids used for CFD. **g**, CFD grid and time-step independence was verified after performing simulations with variable cell density and time-step intervals.